How Uncertainties in Relative Humidity Drive the Spread in the Relationship between Outgoing Longwave Radiation and Surface Temperature Across CMIP6 Models

Jing Feng [1], David Paynter [2], Chenggong Wang [1], Raymond Menzel [2]

[1] Atmospheric and Oceanic Sciences Program, Princeton University, 300 Forrestal Road, Princeton, 08540-6654, New Jersey, United States

[2] Geophysical Fluid Dynamics Laboratory, 201 Forrestal Road, Princeton, 08540-6649, New Jersey, United States

E-mail: `jing.feng@princeton.edu`

June 2023

Abstract. The Earth's global radiation budget depends critically on the relationship between outgoing longwave radiation (OLR) and surface temperature (Ts). Above 270 K, which represents 89% of the surface of Earth, we find that linearity poorly represents the OLR-TS relationship. Although the AMIP runs of CMIP6 models largely capture the linearity of OLR and Ts, there is considerable variation in how they represent this departure from linearity.

In this study, we investigate physical mechanisms that control the OLR-Ts relationship seen in ERA5 reanalysis and CMIP6 models by using accurate radiative transfer calculations. Our study identifies three key mechanisms to explain both the linearity and departure from linearity of OLR-Ts relationship. The first is the total infrared opacity of the atmosphere, which accounts for 60% of the observed OLR-Ts linear slope. The second is changes in atmospheric emission induced by a foreign pressure effect on absorption lines (of water vapor and other greenhouse gases) and continuum absorption of water vapor, which accounts for 30% of the linear slope. The third is changes in atmospheric emission induced by variations in relative humidity, particularly in the mid-troposphere (250 to 750 hPa), which determines the non-linearity in the OLR-Ts relationship and adds to the remaining 10% of the slope. Furthermore, we find that inter-model spread in mid-tropospheric relative humidity explains a large fraction of the differences in OLR across CMIP6 models at given surface temperatures. Our research also shows that the humidity-induced clear-sky OLR curve is synergistically enhanced by clouds owing to a strong correlation between cloud and humidity.

Keywords: outgoing longwave radiation, Earth's radiation balance, climate model

Submitted to: *Environ. Res. Lett.*

1. Introduction

The Earth's climate is regulated by the balance between the net incoming solar radiation and the outgoing longwave radiation (OLR) at the top-of-atmosphere (TOA). The surface of the Earth absorbs energy from incoming solar radiation and emits it in the longwave spectrum. Greenhouse gases and clouds trap the longwave energy radiated from the surface and re-radiate it back to space, controlling the OLR at the TOA. Any additional energy input leads to an increase in the planet's surface temperature (Ts), which is a key quantity for evaluating the potential impacts of climate change on natural and human systems. Understanding the global relationship between OLR and Ts is vital for comprehending the radiation balance of the present-day climate and serves as an important indicator of future climate change.

The relationship between outgoing longwave radiation (OLR) and surface temperature (Ts) has been extensively studied using Earth system models and observational data. Previous research has revealed that over Earth's surface, the OLR exhibits a near-linear relationship with Ts, characterized by a regression coefficient of approximately 2 $Wm^{-2}K^{-1}$ under clear-sky conditions [1, 2, 3]. This overall linearity is attributed to the greenhouse effect of water vapor, which is predominantly influenced by Ts and offsets the growth curve in surface thermal emission [2]. However, it is important to note that OLR is not solely controlled by Ts, as it is also sensitive to atmospheric conditions and clouds [4, 5, 6, 7, 8, 9, 10, 11, 12]. Consequently, stronger deviations from a simple linear function over Ts are observed in subtropical and tropical regions [13], exhibiting seasonal [14] and inter-annual variations [15], as well as under global warming scenarios [16, 17].

This study investigates the key atmospheric conditions that shape the observed OLR over the present-day Earth in Sections 2 and 3 and the causes of the inter-model spread in OLR in Section 4. The results are summarized and discussed in Section 5.

2. The OLR-Ts Relationship in the Present-day Earth

OLR is jointly determined by the opacity of the atmosphere and the thermal emissions from both the surface and the atmosphere. Mathematically, it can be expressed as follows:

$$\begin{aligned} OLR &= \int_{\upsilon} \mathfrak{T}_{\upsilon} B_{\upsilon}(T_s) d\upsilon + \int_{\upsilon} E_{\upsilon} d\upsilon \\ &= \bar{\mathfrak{T}} B(T_s) + E \end{aligned} \tag{1}$$

Here, T_s represents the surface temperature, υ denotes the spectral frequency, $\mathfrak{T}_{\upsilon}$ and E_{υ} refer to the transmission through the atmosphere and atmospheric emission at each spectral frequency, respectively. $B(\upsilon, T_s)$ represents the black-body emission at frequency υ, determined by Planck function of temperature. The terms $E = \int_{\upsilon} E_{\upsilon} d\upsilon$ and $B = \int_{\upsilon} B_{\upsilon} d\upsilon$ correspond to the integrated atmospheric emission and black-body

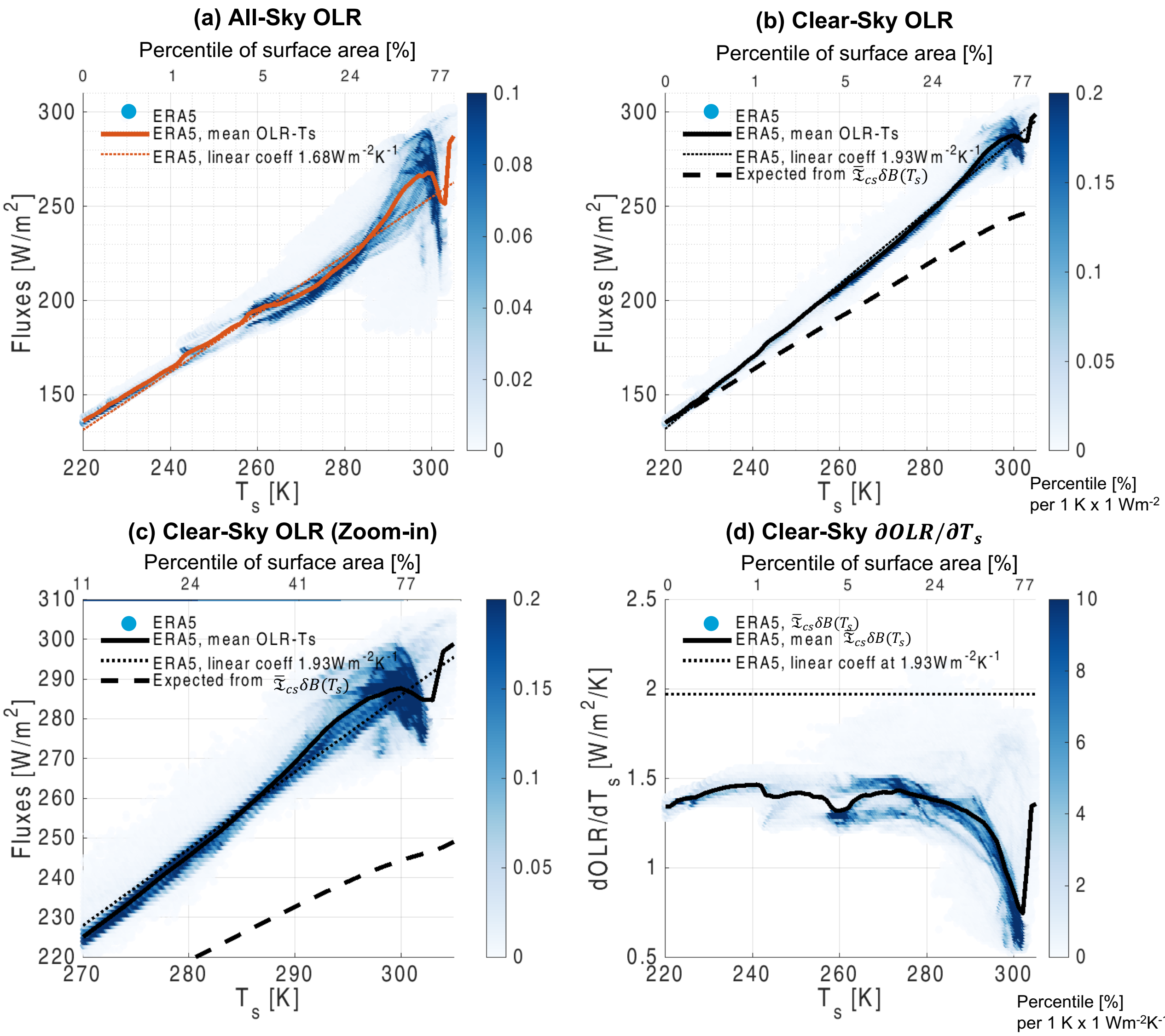

Figure 1. (a) All-sky and (b) clear-sky outgoing longwave radiation (OLR) in W/m^2 as a function of local surface temperature (T_s) in K, based on multi-year-mean gridded ERA5 reanalysis from 1998 to 2014. The color represents the percentile of data grids falling within each 1 K $\times$ 1 W/m^2 box over the globe. The solid curves show the mean OLR at each 1 K T_s bin from ERA5. The dotted lines represent the linear regression lines of OLR to T_s, with the regression coefficients labeled. The top x-axis displays the percentiles of the surface area colder than 220, 240, 260, 280, and 300 K based on multi-year-mean Ts. Panel (c) is similar to (b), but it covers the Ts range from 270 K to 305 K, corresponding to 89 % of the surface area. Panel (d) is similar to (b) but represents the clear-sky surface contribution to the OLR-Ts slope, evaluated as $\delta\bar{\mathfrak{T}}B(T_s)$ at every grid, and the mean of it at every Ts bin is integrated into the dashed curves in panels (b) and (c).

emission, respectively. The term $\bar{\mathfrak{T}} = \int_v \mathfrak{T}_v B_v(T_s) dv / B(T_s)$ represents the broadband transmission, indicating the rate at which surface emission transmits to space.

Under clear-sky conditions, [2] proposed that the rate at which surface emission transmits to space determines the rate at which OLR increases with Ts. They suggested that OLR tends to increase linearly with T_s rather than following a quadratic growth curve following $B(T_s)$, and that this linearity arises because the quadratic growth curve rate is offset by the rate at which water vapor transmittance ($\sim \bar{\mathfrak{T}}_{cs}$) decreases with Ts.

With ERA5 reanalysis [18] and line-by-line radiative transfer (GRTCODE), we can quantitatively examine how well the surface contribution can explain the observed and simulated OLR-Ts relationship on present-day Earth. Figure 1(a) shows the multi-year-mean OLR at every grid point on Earth as a function of Ts, based on the reanalysis, with the global distribution of multi-year-mean Ts presented in Figure B1. Figure 1(a) suggests a near-linear increase in OLR with Ts, with more pronounced deviations from linearity in warmer regions. The linear regression slope is 1.93 $\mathrm{Wm^{-2}K^{-1}}$ under clear-sky conditions, consistent with the findings of [2], and 1.68 $\mathrm{Wm^{-2}K^{-1}}$ under all-sky conditions.

To understand what controls the increase in OLR (δOLR) in response to a Ts increase (δT_s) under the impact of the co-variation of atmospheric transmittance and emission with Ts ($\delta\bar{\mathfrak{T}}$ and δE), we analytically decompose δOLR as follows:

$$\delta OLR = \underbrace{\bar{\mathfrak{T}}[B(T_s + \delta T_s) - B(T_s)]}_{\bar{\mathfrak{T}}\delta B(T_s)} + \delta\bar{\mathfrak{T}} B(T_s + \delta T_s) + \delta E \tag{2}$$

In this expression, $\bar{\mathfrak{T}}\delta B(T_s)$ represents the change in OLR resulting from a one-sided partial radiative perturbation in T_s, equivalent to the surface contribution proposed in [2]. When $\delta T_s = 1\mathrm{K}$, this term is known as the "surface Planck feedback" [2, 19, 20] or the surface temperature kernel [10, 21, 22] at local grid points.

To compute $\bar{\mathfrak{T}}_{cs}\delta B(T_s)$ at each grid point, we conduct line-by-line radiative transfer calculations using GRTCODE, as described in Data and Method. Similar to Figure 1(a), Figure 1(d) presents $\bar{\mathfrak{T}}_{cs}\delta B(T_s)$ as a function of Ts. When compared to the observed clear-sky OLR-Ts slope, however, $\bar{\mathfrak{T}}_{cs}\delta B(T_s)$ is significantly lower and decreases further with increasing Ts. The magnitude of $\bar{\mathfrak{T}}_{cs}\delta B(T_s)$ is highly consistent with the line-by-line calculations conducted in [20] and the clear-sky surface temperature kernel available in publicly accessible datasets [10, 21].

To determine how much OLR increase from a reference Ts due to the surface contribution, we integrate $\bar{\mathfrak{T}}$ (as a function of Ts) over $B(T_s)$ as:

$$\Delta OLR_{sfc}(T_i) = \int_{T_s=270}^{T_s=T_i} \bar{\mathfrak{T}} dB(T_s) \tag{3}$$

The derived $\Delta OLR_{cs,sfc}$ is then utilized to "predict" the clear-sky OLR curve and is shown as the black dotted curve in Figure 1(b,c), following [2], using reference Ts values of 220 K. It becomes evident that ΔOLR_{sfc} significantly underestimates the OLR slope, regardless of the reference Ts. Thus, the surface contribution $\bar{\mathfrak{T}}_{cs}\delta B(T_s)$ alone cannot explain the linear OLR-Ts relationship to the first order. In particular, in regions with Ts above 290 K, $\bar{\mathfrak{T}}_{cs}\delta B(T_s)$ is less than 1 $\mathrm{Wm^{-2}K^{-1}}$. Given its magnitude, which is much smaller than the actual OLR-Ts slope observed in these regions [3], $\bar{\mathfrak{T}}_{cs}\delta B(T_s)$ cannot account for the observed OLR-Ts slope, regardless of the grid points being selected from this region. A significant portion of the linearity must arise from the atmospheric contribution through $\delta\bar{\mathfrak{T}}B(T_s + \delta T_s) + \delta E$ in Equation 2.

Moreover, it is important to note that because Ts is not evenly distributed across the planet, using Ts as a coordinate exaggerates the linearity of the OLR-Ts relationship. In reality, regions with non-linearity (Ts > 270 K) cover 89% of Earth's surface area. To address this visual artifact, Figure 1(c), as well as the following context of this paper, focuses on regions with Ts warmer than 270 K, roughly from 60^o north to south (Figure B1). As Ts increases, OLR deviates more strongly from a simple linear function over Ts, and this deviation pattern is well described by the mean OLR at each Ts bin. The mean OLR-Ts curves under clear-sky and all-sky conditions appear similar, with a steeper gradient in regions with Ts above 270 K, reaching a peak at 298 K, and then a dip at 302 K. From the sea surface temperature shown in Figure B1, we find that the OLR peak is reached in the subtropical ocean and tropical cold pool, corresponding to dry, subsidence region. The dip is reached in the tropical warm pool, corresponding to moist, convective regions. The observed OLR curvature cannot be explained by the surface contribution.

3. How Atmosphere Shapes the Clear-sky OLR-Ts Relationship

While the surface contribution to OLR, which can be directly computed from radiative transfer models, fails to effectively explain the observed OLR-Ts relationship, the atmospheric contribution poses a challenge due to the interplay between transmission, emission, and perturbations to them. Alternatively, we infer the sum of atmospheric contributions from the OLR increase not explained by ΔOLR_{sfc} as ΔOLR_{atm}:

$$\begin{aligned}\Delta OLR(T_i) &= OLR(T_s = T_i) - OLR(T_s = 270)\\ \Delta OLR_{atm}(T_i) &= \Delta OLR(T_i) - \Delta OLR_{sfc}(T_i)\end{aligned} \tag{4}$$

Figure 2 shows the ΔOLR_{cs}, $\Delta OLR_{cs,sfc}$, and $\Delta OLR_{cs,atm}$ based on monthly-mean reanalysis dataset in black curves, with respect to 270 K Ts; similar results but with respect to 220 K are shown in Figure B2. In the 270 to 305 K Ts range, the clear-sky OLR-Ts slope is at 2.11 $\mathrm{Wm^{-2}K^{-1}}$ (Figure 2(a)), 1.27 $\mathrm{Wm^{-2}K^{-1}}$ of it is explained by the surface term (Figure 2(b)). Figure 2(c) reveals that the atmospheric term not only contributes to 0.85 $\mathrm{Wm^{-2}K^{-1}}$ of the linear slope but also controls the curved OLR-Ts relationship.

Earlier studies [13] have depicted a "radiator fin" in dry, descending regions and a "radiator furnace" in moist, ascending regions, which highly aligns with the key feature observed in Figure 1. The proposed explanation was that higher OLR occurs in drier regions because the atmosphere is more transparent in the longwave spectrum with less water vapor content, allowing for more efficient heat loss to space. Thus it would appear that the transmission through the entire atmospheric column ($\bar{\mathfrak{T}}$ and $\delta\bar{\mathfrak{T}}$) might explain the observed OLR-Ts curve. On the other hand, it is well-known that OLR is quantitatively sensitive to layer-by-layer perturbations in atmospheric humidity [5, 6, 7, 9, 11, 17, 12]. However, it is unclear whether the OLR sensitivities to perturbations in global-mean or local grid points would lead to a conclusion that differs from the first-order picture in which transmission through the entire atmospheric column shapes the OLR-Ts relationship.

To understand how the complex atmospheric properties shape the observed OLR-Ts relationship, we construct a set of atmospheric columns using ERA5 reanalysis dataset. At each 1-K Ts bin, we build three cases, as summarized in Table 1, that have identical temperature and ozone profiles, well-mixed greenhouse gas contents, stratospheric water vapor, and column-integrated water vapor in the troposphere (CIWV), but distribute CIWV differently in vertical levels.

In Case a, the tropospheric RH is fixed at 40%, while the bottom layer humidity is adjusted to achieve the prescribed CIWV. Case b assumes vertically-uniform tropospheric RH within each Ts bin, with the RH values inferred from the prescribed CIWV. Case c utilizes the mean RH profile at each Ts bin derived from ERA5 and should largely reproduce the mean OLR of each bin. Given that the transmission through the entire atmospheric column is primarily influenced by CIWV, we expect the mean transmission ($\bar{\mathfrak{T}}$) and changes in transmission ($\delta\bar{\mathfrak{T}}$) to be similar across these different cases.

Following this idea, we conduct clear-sky radiative transfer calculations for three cases at every Ts bin using MODTRAN 5.2 [23] (see Data and Method) to derive the OLR-Ts relationship, ΔOLR_{cs}, the surface component, $\Delta OLR_{cs,sfc}$, and the atmospheric component, $\Delta OLR_{cs,atm}$. As expected, the surface component overlaps among the three cases, primarily owing to the dominant impact of CIWV on the magnitude of $\bar{\mathfrak{T}}$, further suggesting the similarity of $\delta\bar{\mathfrak{T}}$ across these cases. Consequently, any discrepancies observed in the OLR-Ts relationship among the three cases can be attributed solely to changes in atmospheric emission. These OLR-Ts relationships and their differences are used to elucidate how atmospheric conditions shape the slope and curvature observed in the OLR-Ts relationship.

Table 1. A summary of atmospheric columns constructed at every 1-K surface temperature bin with different vertical distribution of tropospheric humidity. Temperature profiles, well-mixed greenhouse gases, O_3, and tropospheric column-integrated water vapor (CIWV), and stratospheric humidity (above 200 hPa) are the same in Cases a, b, and c as in ERA5 multi-year-mean. Clear-sky radiative transfer calculations are conducted at every Ts bin using MODTRAN 5.2 [23] at 1 cm^{-1} spectral resolution to obtain OLR, ΔOLR_{sfc}, and ΔOLR_{atm} presented in Figure 2. ΔOLR_{sfc}, and ΔOLR_{atm} are used to derive the linear regression slope ($\partial OLR_{cs,\mathrm{sfc}}/\partial T_s$ and $\partial OLR_{cs,\mathrm{atm}}/\partial T_s$) and are presented in this table.

Experiments	Temperature	Humidity	$\partial OLR_{cs,\mathrm{sfc}}/\partial T_s$	$\partial OLR_{cs,\mathrm{atm}}/\partial T_s$
Atmospheric Columns with Different Tropospheric Humidity				
a. 40% RH	Multi-year-mean within each Ts bin figure B4(b)	Prescribed CIWV 40% tropospheric RH (except for the bottom layer)	1.30 $Wm^{-2}K^{-1}$	0.62 $Wm^{-2}K^{-1}$
b. Mean RH	Figure B4(b)	Prescribed CIWV Vertically-uniform RH in the troposphere Green curve in Figure B4(a)	1.34 $Wm^{-2}K^{-1}$	0.70 $Wm^{-2}K^{-1}$
c. RH profile	Figure B4(b)	Vertically-resolved tropospheric RH	1.27 $Wm^{-2}K^{-1}$	0.87 $Wm^{-2}K^{-1}$
ERA5	-	-	1.27 $Wm^{-2}K^{-1}$	0.85 $Wm^{-2}K^{-1}$

3.1. Atmospheric Emission Maintains the Near-constant $\partial OLR/\partial T_s$

Figure 2(a) shows that the observed OLR-Ts slope is much steeper than the surface component (Figure 2(b)) could explain, even in Case a when a constant tropospheric RH is maintained. This result should not be taken for granted because it breaks 'Simpson's law' suggested by previous studies [24, 19], which states that if the water vapor mass at any given temperature level is constant (i.e., constant RH) regardless of Ts, then thermal emission from water vapor should be largely constant even when the surface warms. Figure 3(a)) shows that Case a maintains a near-constant water vapor path (WVP) at temperature levels, but $\Delta OLR_{cs,atm}$ still increases significantly with Ts. Similar magnitude in $\Delta OLR_{cs,atm}$ is found even when water vapor is held as the only greenhouse gas in Figure B3 for an idealized scenario constructed in Table C1.

To understand why $\Delta OLR_{cs,atm}$ increases with Ts, we examine the opacity of water vapor of Case a in Figure 3(b). It shows that with constant RH $\Delta OLR_{cs,atm}$ increases with Ts because the opacity of water vapor is not constant for the same mass of water vapor. The Simpson's law would hold only if the temperature-pressure relationship is perfectly maintained, as depicted in a hypothetical scenario 'Simpson' built in Table C1 and Figure B3(c), which is unrealistic in Earth's atmosphere. Due to a near-constant surface air pressure, a foreign pressure effect on the thermal emission of water vapor is introduced, reducing the absorption coefficient per unit mass at a given air temperature [25, 26, 20]. Consequently, the opacity contour shifts to warmer atmospheric layers (Figure 3(b)), leading to an increase in $\Delta OLR_{cs,atm}$ with Ts. The effective emission temperature of the atmosphere follows this shift and increases by approximately 0.25 K for every 1 K increase in Ts (25% of ΔT_s). This rate of emission temperature shift is determined by the Clausius-Clapeyron equation and the hydrostatic balance [27], as demonstrated in Equation 9 of [20]. Therefore, the near-linear relationship between $\Delta OLR_{cs,atm}$ and Ts in Case a arises from the cancellation of the quadratic growth curve

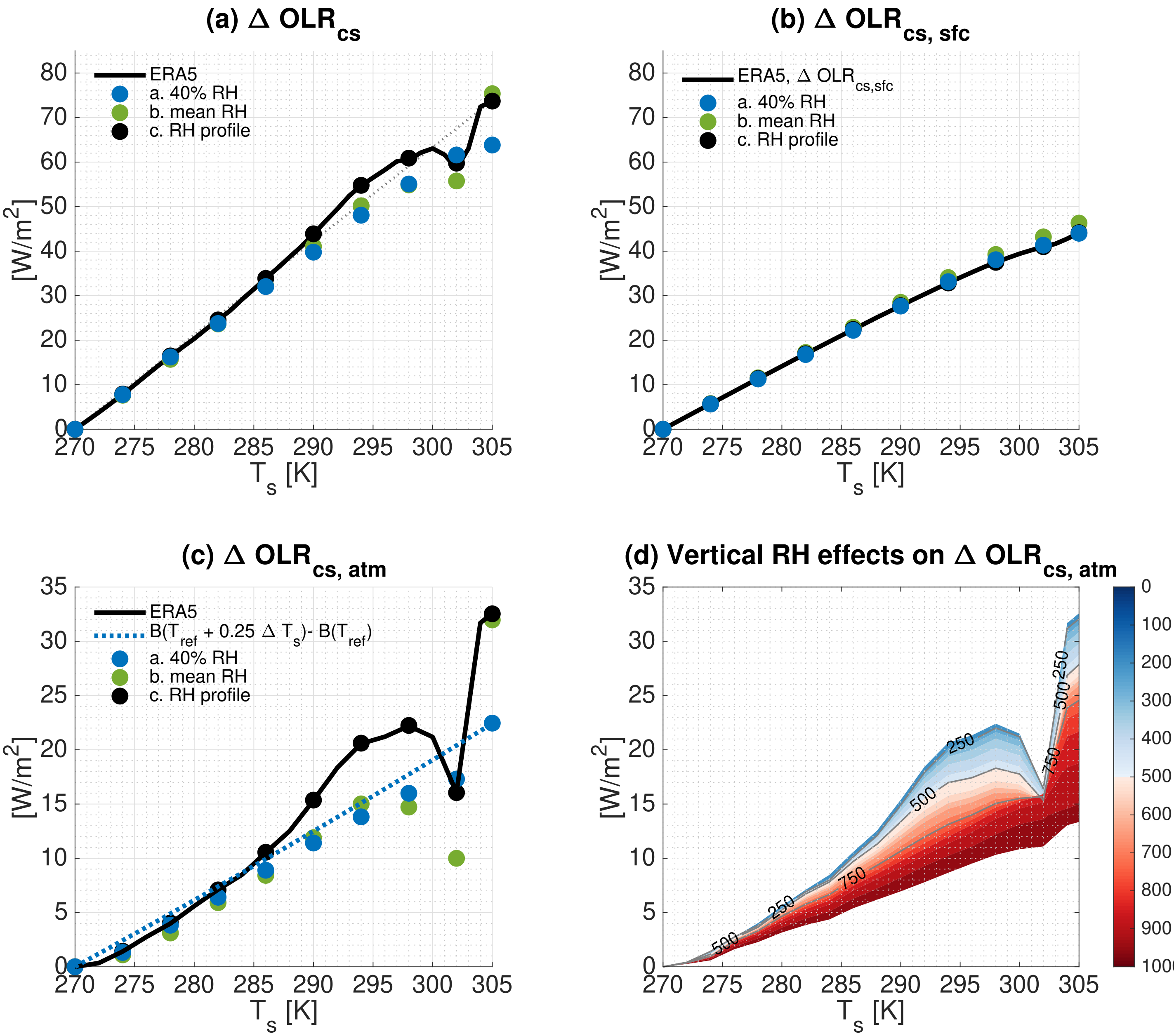

Figure 2. The clear-sky OLR curvature is sourced from atmospheric emission, controlled by the variation in RH with respect to T_s, particularly in the vertical range between 250 and 750 hPa. (a) The black solid curve and the grey-shaded area are the same as Figure 1 but for ΔOLR_{cs}, using ERA5 reanalysis. Markers are color-coded for atmospheric columns constructed with different temperature and humidity conditions as described in Table 1. (b) Same as (a) but for $\Delta OLR_{cs,sfc}$. (c) Same as (a) but for $\Delta OLR_{cs,atm}$. The purple solid curve shows $B(T_{ref} + 0.25\Delta T_s) - B(T_{ref})$ based on Eq. 9 in [20], where T_{ref} is set to be 230 K inferred from the mean atmospheric emission at 270 K Ts. (d) $\Delta OLR_{cs,atm}$ when RH profile from ERA5 is used from surface to TOA layer-by-layer, color-shaded by vertical pressure layer [hPa].

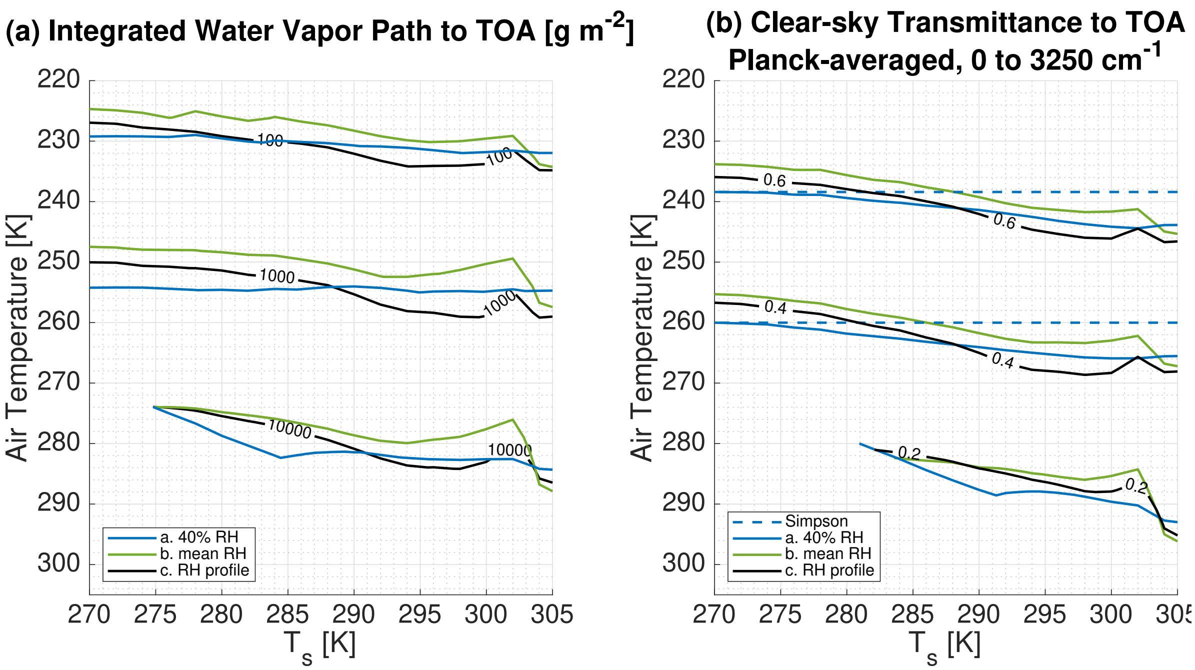

Figure 3. (a) Integrated water vapor path (WVP) [gm^{-2}] from TOA to layer-by-layer atmosphere as a function of air and surface temperatures, for cases with different humidity inputs. (b) The same as (a) except for the atmospheric transmittance with water vapor as the only greenhouse gas (measured from the top-of-atmosphere to the surface, Planck-averaged over 1 to 3250 cm^{-1}).

in $B(T_s)$ by the dampened emission temperature shift, making the observed OLR-Ts relationship much steeper and more linear than the surface contribution could explain.

3.2. Atmospheric Emission Shapes the OLR-Ts Relationship via Relative Humidity Distribution

However, Case a cannot reproduce the curved OLR-Ts relationship even with its total atmospheric transmittance matching the reanalysis. The big discrepancies between Case a and other cases with the same CIWV but varying humidity preclude any major effects from the trapping greenhouse effect of water vapor (via $\bar{\mathfrak{T}}$ and $\delta\bar{\mathfrak{T}}$), suggesting that the atmospheric emission must have played a key role in shaping the observed OLR-Ts curve.

Figure 2 demonstrates that the curved OLR-Ts relationship is better captured in Case b, where RH is uniformly prescribed in every tropospheric layer to yield the mean CIWV at each Ts bin. In this case, the increasing RH from 298 K to 302 K lifts the transmittance contour (Figure 3(b)), making atmospheric emission at colder layers more effective and significantly reducing OLR.

Surprisingly, the mean tropospheric RH alone cannot fully explain the linear slope in $\Delta OLR_{cs,atm}$. Case b underestimates the overall ΔOLR_{cs} and fails to account for the maximum $\Delta OLR_{cs,atm}$ occurring at 298 K instead of 294 K, where the mean tropospheric RH is the lowest (Figure B4(a)). Case c eliminates these discrepancies by using a vertically-resolved RH profile in the troposphere at each Ts bin. Figure 2(d) shows that the WVP with respect to air temperature levels reaches a minimum at 298 K, and the contour curves in the middle troposphere (around 240 to 270 K air temperature levels or 250 to 750 hPa pressure levels) are much steeper than the average troposphere. It suggests that the mean tropospheric RH in Case b inadequately represents the humidity change in the middle troposphere. By considering contributions from realistic RH layer-by-layer from the surface to the top of the atmosphere (TOA) and conducting radiative transfer calculations, we demonstrate in Figure 2(c) that the middle troposphere (between 250 and 750 hPa) significantly influences both the slope and intensity of the $\Delta OLR_{cs,atm}$-Ts curve. While previous studies have recognized the importance of middle-tropospheric humidity using radiative partial perturbation methods and kernels [7, 11, 12], the radiative transfer through the constructed columns proves that the middle-tropospheric humidity is important because it determines the atmospheric emission to space. It also explains why the OLR-Ts relationship appears more linear when grids with conserved middle-tropospheric RH, rather than boundary-layer RH, are chosen [3].

In conclusion, we find that the total transmission alone is insufficient to describe the OLR-Ts relationship (Figure 2(b) versus Figure 2(a)). On one hand, a significant fraction (approximately 40%) of the linear slope in the observed OLR-Ts relationship is attributable to atmospheric thermal emission, primarily from water vapor (Figure B3(a)), which is induced by the pressure-broadening effect and enhanced by variations in tropospheric RH. On the other hand, the curved shape in the OLR-Ts relationship is predominantly due to atmospheric emission: OLR peaks at 298 K because this 1-K surface temperature bin on average corresponds to the driest mid-troposphere, allowing for more effective emission from warmer atmospheric layers rather than just the surface. These key characteristics of the OLR-Ts relationship cannot be reproduced if the column mass of greenhouse gases is prescribed without considering the vertical distribution of RH.

4. The Cause of Inter-model Spread in the Clear-sky OLR Curve

The mean clear-sky OLR at each Ts bin from the AMIP simulation of 24 CMIP6 models is shown in Figure 4(a). The inter-model spread in clear-sky multi-year-mean OLR at given Ts is surprisingly large with the prescribed sea surface temperature in the AMIP experiment. In this section, the cause of inter-model spread in clear-sky OLR at given Ts is examined. In particular, it is intriguing to decompose whether the spread is caused by differences in radiative transfer schemes used by these models or by differences in atmospheric states. Therefore, we perform global clear-sky radiative transfer calculations for 24 CMIP6 models using RTE-RRTMGP [28], as described in Data and Method. The multi-year-mean OLR and transmittance at every model grid point are computed from monthly-mean results. This set of calculations excludes

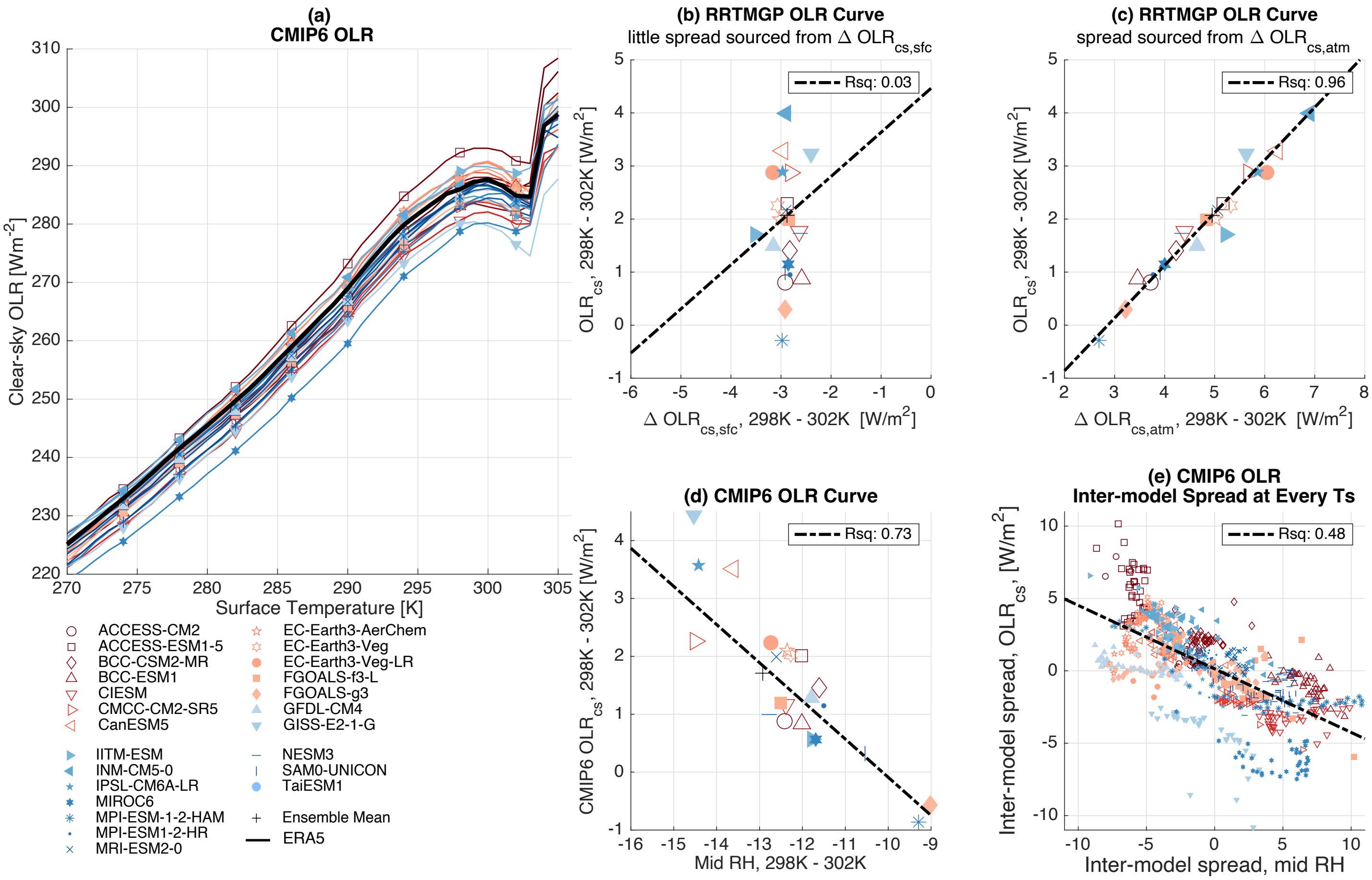

Figure 4. Inter-model spread in the clear-sky OLR-Ts relationship can largely be attributed to differences in mid-tropospheric RH (700 to 300 hPa), as revealed by RRTMGP calculations (b, c) and CMIP6 standard output (d, e) for the period 1998 to 2014, focusing on regions with multi-year-mean temperatures above 270 K. Panel (a) displays the clear-sky OLR as a function of Ts from 24 models. Panels (b), (c), and (d) depict the differences in OLR at 298 K compared to 302 K for each CMIP6 model, with respect to differences in surface OLR ($\Delta OLR_{cs,sfc}$), atmospheric OLR ($\Delta OLR_{cs,atm}$) computed using RRTMGP with CMIP6 inputs (plev19 temperature and humidity profiles), and mid-tropospheric RH derived from CMIP6 fluxes and humidity profiles, respectively. Panel (e) shows the inter-model spread in CMIP6 clear-sky OLR at each 1 K Ts bin as a function of the inter-model spread in mid-tropospheric RH. Dashed lines represent linear correlation regression between the x and y axes in each panel, and the R-squared values indicate the proportion of variation in the y-axis that can be explained by the x-axis.

any discrepancies induced by the treatment of greenhouse gases and biases in radiative transfer schemes.

The spread in clear-sky OLR computed from RRTMGP remains comparable to the standard output from CMIP6 (Figure B5(a)), suggesting a large fraction of the inter-model spread is caused by discrepancies in atmospheric states. Overall, these models exhibit curved shapes in OLR that are highly consistent with ERA5, reaching a maximum around 298 K and a dip around 302 K. However, the strength of this

OLR curvature, evaluated as the OLR contrast between the two Ts bins is quite different across models, as shown in the y axes of Figure 4(b,c,d), ranging from -0.3 to 4 Wm^{-2}. The region between 298 and 302 K spans over the majority of the subtropical and tropical ocean (Figure B1), and is representative of the most dramatic changes in humidity conditions with Ts over the present-day Earth. The magnitude of OLR contrast between the two bins indicates how each model represents the tropical circulation that transports heat and moisture between the moist, ascending "radiator furnace" and the dry, descending "radiator fin" on Earth [13].

Based on RRTMGP calculations and following Section 3, we break down the contribution to the OLR contrast between 298 and 302 K region into the surface ($\Delta OLR_{cs,sfc}$) and atmospheric contributions ($\Delta OLR_{cs,atm}$), as shown in Figure 4(b,c). While the consistency in $\Delta OLR_{cs,sfc}$ across models suggests an overall good agreement in the CIWV, the changes in atmospheric emission do not align well among the CMIP6 models when using the same radiative transfer codes. Combing Figure 4(b) and (c), our results suggest that the inter-model spread in the strength of OLR curvature is primarily sourced from atmospheric emission, potentially due to the mid-tropospheric RH as alluded to in Section 3.2.

Next, we examine whether the inter-model spread in clear-sky OLR can be explained by the mid-tropospheric RH. Figure 4(d) shows that 73 % of the inter-model spread in the clear-sky OLR difference between the 298 K and 302 K regions can be attributed to the inter-model spread in mid-tropospheric RH. If the contrast in the mid-tropospheric RH is too low in one model, the model tends to produce a relatively low or even negative OLR contrast between the subtropical ocean at 298 K and the tropical warm pool at 302 K, due to compensation from the $\Delta OLR_{cs,sfc}$ term at -3 Wm^{-2}. Meanwhile, models with excessively high RH contrast overestimate the OLR contrast between the two regions.

Furthermore, Figure 4(e) shows that, outside of the 298 to 302 K range, the inter-model spread in mid-tropospheric RH explains 48 % of the inter-model spread in OLR at each 1-K bin of surface temperature. It implies that lower clear-sky OLR at a given surface temperature in one model is most likely due to a moister mid-troposphere RH in this model; this finding is consistent with recent studies on the cause of spread in global-mean OLR [29].

5. Discussion

This study reveals a robust and curved relationship between outgoing longwave radiation (OLR) and surface temperature (Ts) in CMIP6 models and ERA5 reanalysis datasets. While the OLR-Ts relationship appears linear within a wide Ts range (220 K to 305 K), this masks the uneven distribution of Ts across the globe and the deviation of OLR from a simple linear relationship in the warmer regions of Earth's surface under both clear- and all-sky conditions. By constructing atmospheric columns based on ERA5 multi-year-mean data, our results explain the key feature in the observed OLR-Ts relationship.

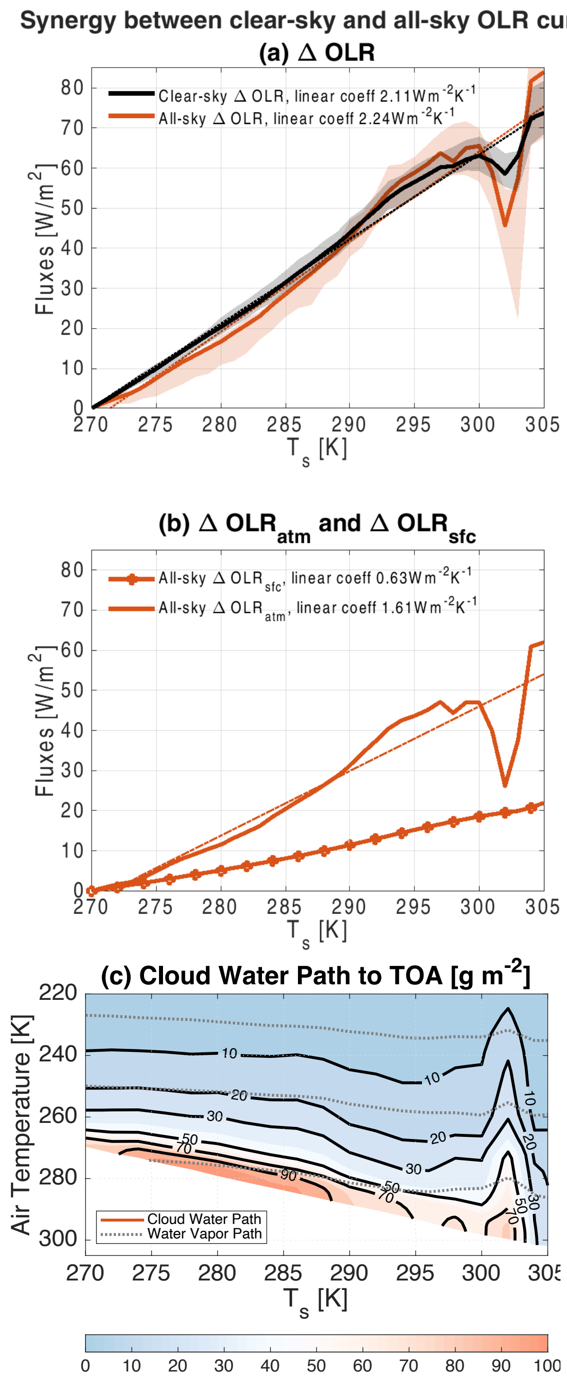

Figure 5. (a) The same as Figure 2(a) for clear-sky (black) and all-sky (red) ΔOLR. Solid curves are ERA5 multi-year-mean and the shaded area represents the 5-95 percentile of multi-year-mean CMIP6 output for AMIP experiments. (b) The same as Figure 2(b,c) for all-sky ΔOLR_{sfc} (solid curve with marker) and ΔOLR_{atm} (solid curve) based on ERA5 multi-year-mean. (c) Similar to Figure 3(a), color-shaded for cloud water vapor to TOA [gm^{-2}] based on ERA5 multi-year-mean. Grey dotted contour curves are WVP, the same as black curves in Figure 3(a).

First, the overall linearity observed in the OLR-Ts relationship is a result of the Clausius-Clapeyron relation, which governs the dependence of humidity on temperature and effectively offsets the quadratic growth curve in blackbody thermal emission from both the surface and the atmosphere. On the one hand, the infrared opacity of water vapor throughout the atmospheric column, as noted in [2], controls the rate at which surface thermal emission escapes to space. On the other hand, the emission temperature from water vapor itself tends to increase by 0.25 K per 1 K of increase of Ts, a rate jointly determined by the Clausius-Clapeyron relation and a pressure-broadening effect on water vapor absorption lines, as explained in [20]. Both the surface and the atmosphere contribute to the linear OLR slope, with their magnitudes compensating for each other depending on atmospheric opacity. In colder and drier regions, the surface contribution is dominant, while in warmer and moister regions, the atmospheric contribution becomes more significant. This finding aligns with previous studies by [20] and [30]. On the present-day Earth, the surface contribution accounts for 60 % and the atmospheric emission via pressure-broadening effect accounts for 30% of the linear slope in the observed clear-sky OLR-Ts relationship.

Second, the variability in tropospheric relative humidity (RH) in the mid-troposphere (250 to 750 hPa vertical range) has a substantial impact on atmospheric thermal emission and contributes to an additional 10% increase in OLR with Ts. Moreover, the spatial variations in mid-tropospheric humidity play a crucial role in the observed non-linearity of the OLR-Ts relationship over the subtropical and tropical oceans, as illustrated in Figure 2(c, d), resulting from the large-scale tropical circulation [13]. We find that OLR over the dry subtropical ocean (around 298 K Ts) is higher than over the moist tropical ocean (around 302 K Ts) because the drier mid-troposphere shifts atmospheric emission to warmer layers (Figure 3(b)), rather than reducing the trapping of surface thermal emission.

Furthermore, our results reveal that CMIP6 models have a remarkably wide spread (up to 10 Wm^{-1}) in multi-year-mean clear-sky OLR at given surface temperatures for AMIP simulations. A main cause of the spread (for regions warmer than 270 K) is found to be model biases in mid-tropospheric RH (Figure 4(c,d)), which can be affected by discrepancies in land surface temperature, microphysics and convective parameterization across models. In addition, we find that a few CMIP6 models may be biased in radiation parameterization and the treatment of well-mixed greenhouse gases, as it clearly diverges from other CMIP6 models (Figure 4(b)) and RRTMGP-computed fluxes (Figure B5(b)). These biases should be carefully examined in the future.

Moreover, based on similar approaches conducted in Section 3, Figure 5(a) shows that the all-sky OLR-Ts curve (ΔOLR) is quite similar to clear-sky, with comparable magnitudes of linear slope for the 270 to 305 K Ts range, and a similar curved shape that deviates from the linear slope among CMIP6 models and the reanalysis. The ΔOLR_{sfc} of ERA5 is computed using the all-sky total atmospheric transmittance and shown in Figure 5(b) based on GRTCODE. With cloud masking effects, ΔOLR_{sfc} can only explain 27 % of the slope in the OLR-Ts relationship. However, the OLR-Ts slope stays comparable to that in the clear-skies because ΔOLR_{atm} is greatly enhanced by clouds and compensates for the masked surface contribution. Furthermore, we show that clouds are in synergy with water vapor when contributing to the atmospheric emission, as the contour plot of the cloud water path from TOA to air temperature levels appears to be largely parallel to the WVP. Consequently, the cloud extinction (proportional to the cloud water path) enhances the clear-sky OLR-Ts curve. The synergy between clear- and all-sky OLR curves indicates that the general circulation from the tropics to poles and across the tropical ocean is important for redistributing the atmospheric energy and moisture to maintaining the observed OLR-Ts relationship in Earth's climate [13, 31, 32].

Availability Statement

The RTE-RRTMGP radiative transfer package is accessible via https://github.com/earth-system-radiation/rte-rrtmgp.git. ERA5 reanalysis dataset and CMIP6 model outputs are accessible via https://www.ecmwf.int/en/forecasts/dataset/ecmwf-reanalysis-v5 and https://pcmdi.llnl.gov/CMIP6/, respectively. Fluxes computed by RRTMGP will be included in an online data repository upon publication.

Acknowledgments

We acknowledge GFDL resources made available for this research. Nadir Jeevanjee and Pu Lin are acknowledged for their comments and suggestions on an internal review of the manuscript. Jing Feng is supported by the NOAA Climate Program Office under grant U8R1ES2/P01. We thank Robert Pincus, Yi Huang, and Ming Cai for helpful discussions on this paper.

Appendix A. Data and Method

This study uses ERA5 reanalysis [18] and CMIP6 model AMIP simulations [33] to examine what shapes the overall OLR-Ts relationship over the present-day Earth, based on the period from 1998 to 2014. The AMIP simulation is an atmosphere-only climate simulation using prescribed sea surface temperature and sea ice concentrations, and historical well-mixed greenhouse gas concentrations.

While OLR fluxes from reanalysis and model outputs are used, we also conduct radiative transfer calculations to explicitly calculate atmospheric transmission of surface emission and atmospheric emission. Three sets of radiative transfer models are used to balance the need for accuracy and efficiency. Monthly-mean ozone profiles and well-mixed greenhouse gas concentrations are used in these models if not otherwise specified. Temperature and humidity profiles from ERA5 and CMIP6 models at every grid point are used to drive the radiative transfer calculations. They consist of 37 model levels for ERA5 and 19 pressure levels for CMIP6 models.

Geophysical Fluid Dynamics Laboratory (GFDL)'s GPU-able Radiative Transfer code (GRTCODE) is a well-benchmarked [34] line-by-line code. It is used to set up a benchmark value for atmospheric transmittance over the present-day Earth. It is computed at every grid point from the year 1998 to 2014 with monthly-mean temperature and humidity profiles from the reanalysis for both clear- and all-sky conditions.

MODTRAN 5.2 [23] is a fast yet accurate band model that has been widely used in atmospheric radiation studies. It is used to compute atmospheric transmittance at every 1 cm^{-1} through constructed temperature and humidity profiles at each Ts bin. With identical atmospheric inputs, the difference in atmospheric transmittance between MODTRAN 5.2 and GRTCODE is within 1 %.

RTE-RRTMGP [28] is a radiative transfer code designed for fast global-scale radiative transfer calculations. It is used to compute broadband fluxes and transmittance at every grid point with multi-year monthly-mean temperature and humidity profiles from AMIP simulations of 24 CMIP6 models and to analyze the cause of intermodel spread in OLR.

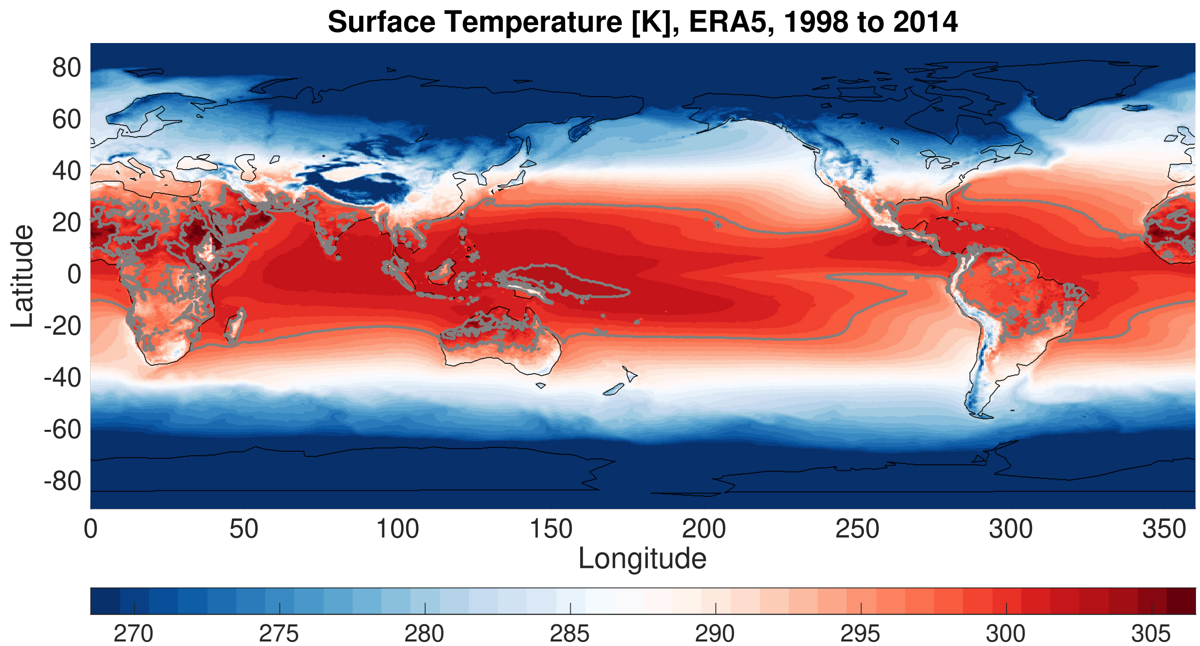

Figure B1. Multi-year-mean surface temperature (Ts) based on ERA5 reanalysis from the year 1998 to 2014. Grey contour marks the 297.5 and 302.5 K Ts.

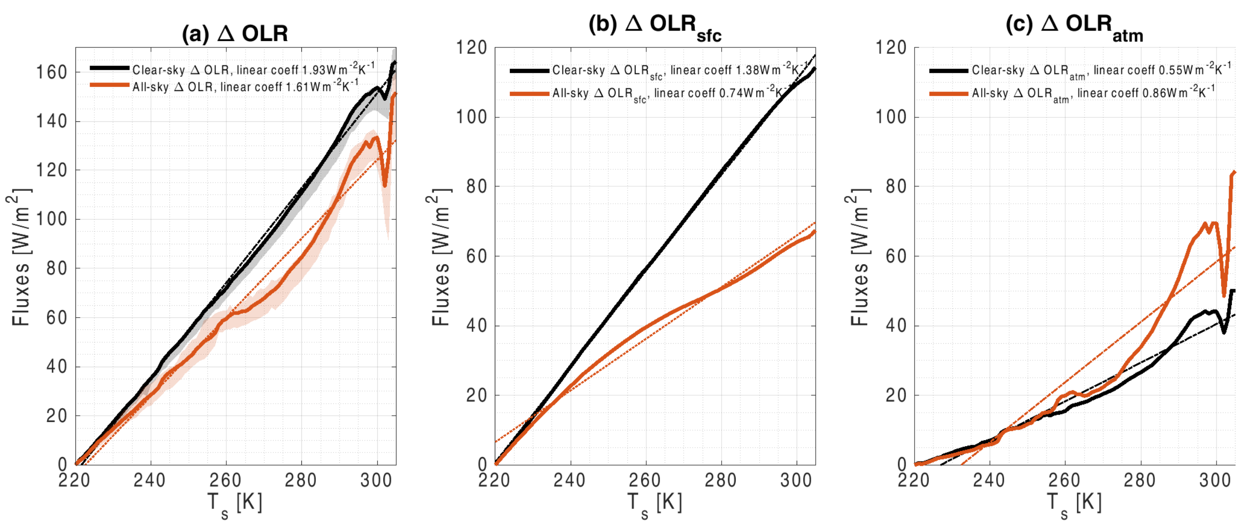

Figure B2. Similar to Figure 2 for ΔOLR (a), ΔOLR_{sfc} (b) and ΔOLR_{atm} (c) for clear-sky OLR (black) and all-sky OLR (red) but using 220 K T_s as a reference point.

397 ## Appendix B. Supplementary Figures

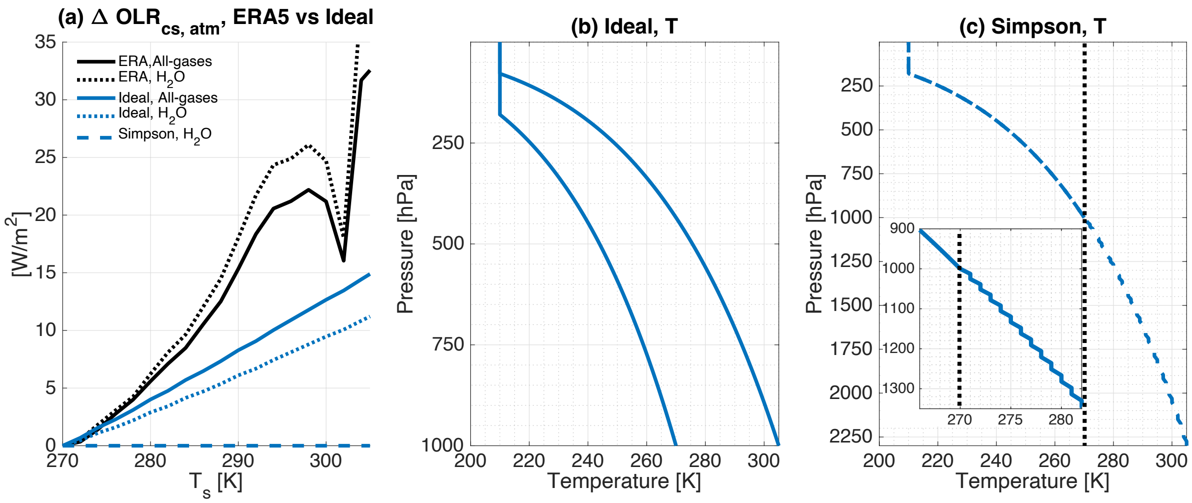

Figure B3. The clear-sky OLR curvature sources from thermal emission of water vapor. The clear-sky Δ OLR$_{cs,atm}$ computed from RRTMGP using temperature and humidity profiles from ERA5 reanalysis datasets as a function of local surface temperature (T_s [K]) with Present-day (PD) greenhouse gas levels (black solid, comparable to the black curve in Figure 2 (c)) and with water vapor as the only greenhouse gas (black dot). Solid and dotted blue curves are similar to black curves but for 'Ideal'. The Blue dashed curve is the 'Simpson' case. (b) Temperature profiles for 'Ideal' at 270 K and 300 K Ts. (c) Temperature profiles for 'Simpson'. These profiles at different Ts perfectly overlap, and are isothermal for every 1-K atmospheric layer from 270 K air temperature to the surface, as demonstrated in the sub-panel on the bottom left.

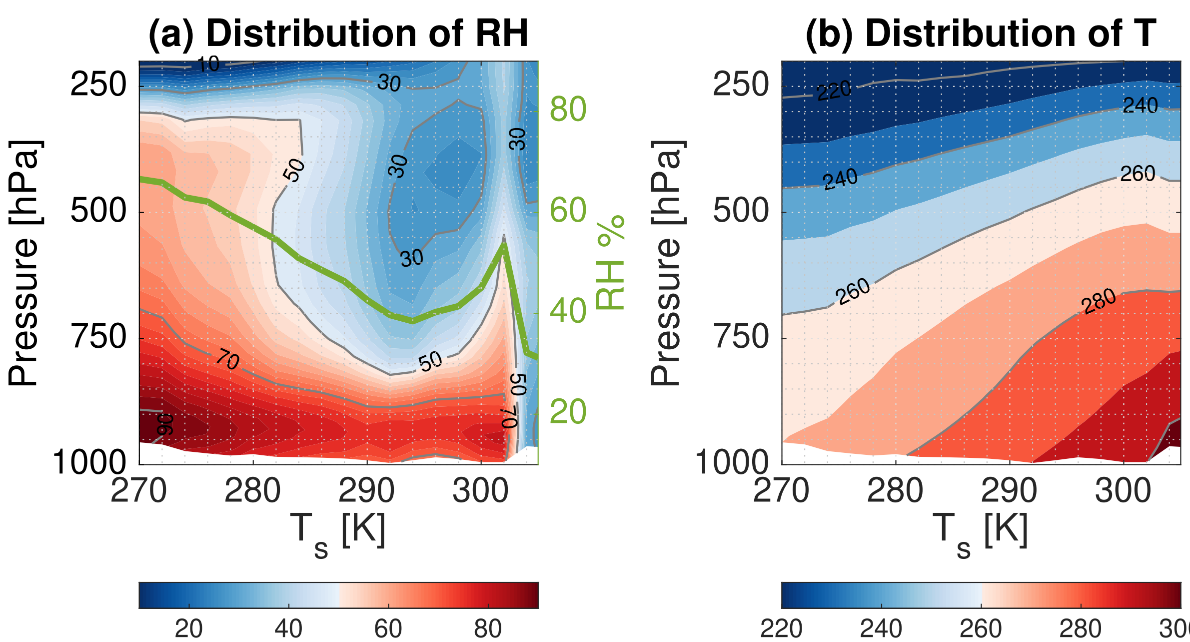

Figure B4. (a) RH (color-shaded) as a function of pressure level and surface temperature from the ERA5 gridded multi-year-mean. The green solid curve shows the tropospheric-mean RH as a function of surface temperature. (b) The same as (a) but for air temperatures. (c) The same as b but for cloud cover.

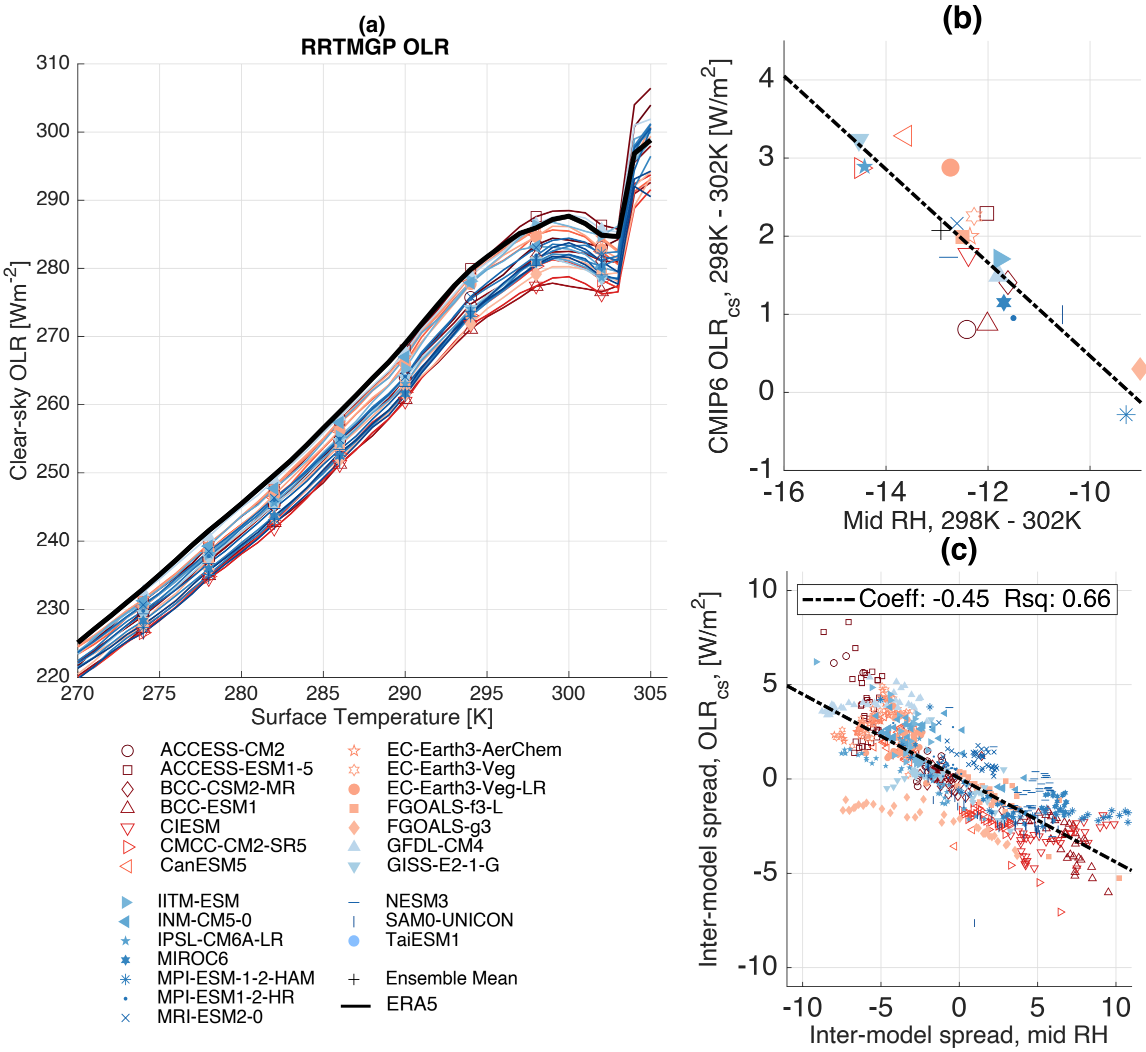

Figure B5. Same as Figure 4(a,d,e) except that OLR fluxes computed from RRTMGP are used.

Appendix C. Supplementary Table

Table C1. Similar to Table 1 but for idealized atmospheric columns with vertically uniform RH and lapse rate in the troposphere.

Experiments	**Temperature**	**Humidity**	$\boldsymbol{\partial OLR_{cs,\mathrm{sfc}}/\partial T_s}$	$\boldsymbol{\partial OLR_{cs,\mathrm{atm}}/\partial T_s}$
Ideal	Uniform tropospheric lapse rate Surface pressure at 1000 hPa Figure B3(b)	40% tropospheric RH	1.40 $\mathrm{Wm^{-2}K^{-1}}$	0.43 $\mathrm{Wm^{-2}K^{-1}}$
Simpson	Same as Ideal, except that the 270 K air is at 1000 hPa, regardless of the actual Ts Figure B3(c)	Same as Ideal	1.25 $\mathrm{Wm^{-2}K^{-1}}$	0 $\mathrm{Wm^{-2}K^{-1}}$

References

[1] MI Budyko, NA Yefimova, LI Aubenok, and LA Strokina. The heat balance of the surface of the earth. *Soviet Geography*, 3(5):3–16, 1962.

[2] Daniel DB Koll and Timothy W Cronin. Earth's outgoing longwave radiation linear due to h2o greenhouse effect. *Proceedings of the National Academy of Sciences*, 115(41):10293–10298, 2018.

[3] Yi Zhang, Nadir Jeevanjee, and Stephan Fueglistaler. Linearity of outgoing longwave radiation: From an atmospheric column to global climate models. *Geophysical Research Letters*, 47(17):e2020GL089235, 2020.

[4] RT Wetherald and S Manabe. Cloud feedback processes in a general circulation model. *Journal of the Atmospheric Sciences*, 45(8):1397–1416, 1988.

[5] Richard Philip Allan, Keith Peter Shine, A Slingo, and JA Pamment. The dependence of clear-sky outgoing long-wave radiation on surface temperature and relative humidity. *Quarterly Journal of the Royal Meteorological Society*, 125(558):2103–2126, 1999.

[6] S Bühler, A Von Engeln, E Brocard, V John, T Kuhn, and P Erikson. The impact of humidity and temperature variations on clear–sky outgoing longwave radiation. *Journal of Geophysical Research. Submitted*, 2004.

[7] Yi Huang, V Ramaswamy, and Brian Soden. An investigation of the sensitivity of the clear-sky outgoing longwave radiation to atmospheric temperature and water vapor. *Journal of Geophysical Research: Atmospheres*, 112(D5), 2007.

[8] Yi Huang and V Ramaswamy. Observed and simulated seasonal co-variations of outgoing longwave radiation spectrum and surface temperature. *Geophysical Research Letters*, 35(17), 2008.

[9] AE Dessler, P Yang, J Lee, J Solbrig, Z Zhang, and K Minschwaner. An analysis of the dependence of clear-sky top-of-atmosphere outgoing longwave radiation on atmospheric temperature and water vapor. *Journal of Geophysical Research: Atmospheres*, 113(D17), 2008.

[10] Brian J Soden, Isaac M Held, Robert Colman, Karen M Shell, Jeffrey T Kiehl, and Christine A Shields. Quantifying climate feedbacks using radiative kernels. *Journal of Climate*, 21(14):3504–3520, 2008.

[11] Shiv Priyam Raghuraman, David Paynter, and V Ramaswamy. Quantifying the drivers of the clear sky greenhouse effect, 2000–2016. *Journal of Geophysical Research: Atmospheres*, 124(21):11354–11371, 2019.

[12] Theresa Lang, Ann Kristin Naumann, Bjorn Stevens, and Stefan A Buehler. Tropical free-tropospheric humidity differences and their effect on the clear-sky radiation budget in global storm-resolving models. *Journal of Advances in Modeling Earth Systems*, 13(11):e2021MS002514, 2021.

[13] R Thermostates Pierrehumbert. Thermostats, radiator fins, and the local runaway greenhouse. *Journal of the atmospheric sciences*, 52(10):1784–1806, 1995.

[14] Benjamin DG Richards, Daniel DB Koll, and Timothy W Cronin. Seasonal loops between local outgoing longwave radiation and surface temperature. *Geophysical Research Letters*, 48(17):e2021GL092978, 2021.

[15] Andrew E Dessler, Thorsten Mauritsen, and Bjorn Stevens. The influence of internal variability on earth's energy balance framework and implications for estimating climate sensitivity. *Atmospheric Chemistry and Physics*, 18(7):5147–5155, 2018.

[16] Jonah Bloch-Johnson, Maria Rugenstein, Martin B Stolpe, Tim Rohrschneider, Yiyu Zheng, and Jonathan M Gregory. Climate sensitivity increases under higher co2 levels due to feedback temperature dependence. *Geophysical Research Letters*, 48(4):e2020GL089074, 2021.

[17] Stella Bourdin, Lukas Kluft, and Bjorn Stevens. Dependence of climate sensitivity on the given distribution of relative humidity. *Geophysical Research Letters*, 48(8):e2021GL092462, 2021.

[18] Hans Hersbach, Bill Bell, Paul Berrisford, Shoji Hirahara, András Horányi, Joaquín Muñoz-Sabater, Julien Nicolas, Carole Peubey, Raluca Radu, Dinand Schepers, et al. The era5 global reanalysis. *Quarterly Journal of the Royal Meteorological Society*, 146(730):1999–2049, 2020.

[19] Nadir Jeevanjee, Daniel DB Koll, and Nicholas Lutsko. "simpson's law" and the spectral cancellation of climate feedbacks. *Geophysical Research Letters*, 48(14):e2021GL093699, 2021.

[20] Jing Feng, David Paynter, and Raymond Menzel. How a stable greenhouse effect on earth is maintained under global warming. *Journal of Geophysical Research: Atmospheres*, 128(9):e2022JD038124, 2023.

[21] Yi Huang, Yan Xia, and Xiaoxiao Tan. On the pattern of co2 radiative forcing and poleward energy transport. *Journal of Geophysical Research: Atmospheres*, 122(20):10–578, 2017.

[22] Ryan J Kramer, Alexander V Matus, Brian J Soden, and Tristan S L'Ecuyer. Observation-based radiative kernels from cloudsat/calipso. *Journal of Geophysical Research: Atmospheres*, 124(10):5431–5444, 2019.

[23] Alexander Berk, Gail P Anderson, Prabhat K Acharya, Lawrence S Bernstein, Leon Muratov, Jamine Lee, Marsha Fox, Steve M Adler-Golden, James H Chetwynd, Michael L Hoke, et al. Modtran 5: a reformulated atmospheric band model with auxiliary species and practical multiple scattering options: update. In *Algorithms and technologies for multispectral, hyperspectral, and ultraspectral imagery XI*, volume 5806, pages 662–667. SPIE, 2005.

[24] Sir George Clarke Simpson. Some studies in terrestrial radiation. *Memoirs of the royal meteorological society*, 11(16):69–95, 1928.

[25] RM Goody and YL Yung. Atmospheric radiation, 519 pp, 1989.

[26] DJ Paynter and V Ramaswamy. An assessment of recent water vapor continuum measurements upon longwave and shortwave radiative transfer. *Journal of Geophysical Research: Atmospheres*, 116(D20), 2011.

[27] John M Wallace and Peter V Hobbs. *Atmospheric science: an introductory survey*, volume 92. Elsevier, 2006.

[28] Robert Pincus, Eli J Mlawer, and Jennifer S Delamere. Balancing accuracy, efficiency, and flexibility in radiation calculations for dynamical models. *Journal of Advances in Modeling Earth Systems*, 11(10):3074–3089, 2019.

[29] Han Huang and Yi Huang. Diagnosing the radiation biases in global climate models using radiative kernels. *Authorea Preprints*, 2023.

[30] Daniel DB Koll, Nadir Jeevanjee, and Nicholas J Lutsko. An analytic model for the clear-sky longwave feedback. *Journal of the Atmospheric Sciences*, 2023.

[31] Yen-Ting Hwang and Dargan MW Frierson. Increasing atmospheric poleward energy transport with global warming. *Geophysical Research Letters*, 37(24), 2010.

[32] Ming Cai, Jie Sun, Feng Ding, Wanying Kang, and Xiaoming Hu. The quasi-linear relation between planetary outgoing longwave radiation and surface temperature: a climate footprint of radiative and non-radiative processes. *Journal of the Atmospheric Sciences*, 2023.

[33] Veronika Eyring, Sandrine Bony, Gerald A Meehl, Catherine A Senior, Bjorn Stevens, Ronald J Stouffer, and Karl E Taylor. Overview of the coupled model intercomparison project phase 6 (cmip6) experimental design and organization. *Geoscientific Model Development*, 9(5):1937–1958, 2016.

[34] Robert Pincus, Stefan A Buehler, Manfred Brath, Cyril Crevoisier, Omar Jamil, K Franklin Evans, James Manners, Raymond L Menzel, Eli J Mlawer, David Paynter, et al. Benchmark calculations of radiative forcing by greenhouse gases. *Journal of Geophysical Research: Atmospheres*, 125(23):e2020JD033483, 2020.